

This is the accepted manuscript made available via CHORUS. The article has been published as:

Structural and electronic phase transitions of ThS_2 from first-principles calculations

Yongliang Guo, Changying Wang, Wujie Qiu, Xuezhi Ke, Ping Huai, Cheng Cheng, Zhiyuan Zhu, and Changfeng Chen

Phys. Rev. B **94**, 134104 — Published 7 October 2016

DOI: [10.1103/PhysRevB.94.134104](https://doi.org/10.1103/PhysRevB.94.134104)

Structural and electronic phase transitions of ThS₂ from first-principles calculations

Yongliang Guo,^{1,2} Changying Wang,² Wujie Qiu,¹ Xuezhi Ke,^{1,*}
Ping Huai,^{2,†} Cheng Cheng,² Zhiyuan Zhu,² and Changfeng Chen^{3,‡}

¹*Department of Physics, East China Normal University, Shanghai 200241, China*

²*Shanghai Institute of Applied Physics, Chinese Academy of Sciences, Shanghai 201800, China*

³*Department of Physics and High Pressure Science and Engineering Center,
University of Nevada, Las Vegas, Nevada 89154, USA*

Thorium and its compounds have received considerable attention in recent years due to the renewed interest in developing the thorium fuel cycle as an alternative nuclear energy technology. There is pressing current need to explore the physical properties essential to the fundamental understanding and practical application of these materials. Here we report on a computational study of thorium disulfide (ThS₂), which plays an important role in the thorium fuel reprocessing cycle. We have employed the density functional theory and evolutionary structure search methods to determine the crystal structures, electronic band structures, phonon dispersions and density of states, and thermodynamic properties of ThS₂ under various pressure and temperature conditions. Our calculations identify several crystalline phases of ThS₂ and a series of structural phase transitions induced by pressure and temperature. The calculated results also reveal electronic phase transitions from the semiconducting state in the low-pressure phases of ThS₂ in the *Pnma* and *Fm $\bar{3}$ m* symmetry to the metallic state in the high-pressure phases of ThS₂ in the *Pnma* and *I4/mmm* symmetry. These results explain the experimental observation of the thermodynamic stability of the *Pnma* phase of ThS₂ at the ambient conditions and a pressure-induced structural phase transition in ThS₂ around 40 GPa. Moreover, the present study reveals considerable additional information on the structural and electronic properties of ThS₂ in a wide range of pressure and temperature. Such information provides key insights into the fundamental material behavior and the underlying mechanisms that lay the foundation for further exploration and application of ThS₂.

PACS numbers: 61.50.Ks, 62.50.-p, 63.20.D-, 71.20.-b

Keywords: Phase transition; Phonon dispersion; Elastic constant; Semiconductor-metal transition; First-principles calculations

I. INTRODUCTION

Thorium and uranium are the only two significantly radioactive elements that occur naturally in large quantities on Earth. While uranium has been the main fuel of choice in conventional reactors, there has been renewed and increasing interest in recent years to further develop thorium based nuclear energy technologies. Thorium has the potential to become a nuclear fuel because ²³²Th, which is not fissile itself, can convert to ²³³U by absorbing slow neutrons¹. A major driving factor for developing the thorium fuel cycle is the concern about the limited resources of uranium², whereas thorium is thought to be three to four times more naturally abundant³⁻⁵. Another advantage of the thorium fuel cycle is that it can be developed to produce negligible amounts of plutonium and fewer long-lived minor actinides than a uranium cycle^{5,6}, thus boosting thorium's potential for improving proliferation resistance and waste characteristics. Research in this field is currently at an early stage and reported results are still limited; but we expect that this field will attract more attention as understanding on relevant fundamental science advances and technological breakthroughs happen. It is therefore important to explore materials and processes relevant to the thorium-based fuel technology.

Crucial to the development of the thorium fuel cycle is a clear understanding of the structural, electronic and thermodynamic properties of thorium and its compounds

that are present at various stages of the fuel cycle. The recovery of thorium from reprocessing the spent nuclear fuel is an important process, and it is achieved by separating and recycling thorium from the spent fuel using the sulfurization method⁷⁻¹² where thorium dioxide can be sulfurized by carbon disulfide at high temperature. The sulfurized material can then be separated from the oxides or metals by the acid leaching method^{10,11}. Several thorium oxides and sulfides appear during the spent fuel reprocessing procedures. Among them is thorium disulfide (ThS₂), which appears as an intermediate phase that serves as an important link in the thorium fuel reprocessing cycle. It is known that ThS₂ has orthorhombic cotunnite-type structure (space group *Pnma*, *Z* = 4)¹³⁻¹⁶, and at high pressures ThS₂ undergoes a structural phase transition around 40 GPa¹⁶. However, details about this phase transition, especially an accurate structural determination of the high-pressure phase, remain unclear. Furthermore, there is a lack of understanding of the electronic and thermodynamic properties of ThS₂ at either ambient or high pressure and temperature conditions. Knowledge about these properties is essential to the understanding of the fundamental material behavior of this compound and its role in the thorium fuel cycle.

In the present work we report on a systematic study of the structural, electronic, lattice dynamic, and thermodynamic properties of ThS₂ over a wide range of pressure and temperature. We first determine the crystal

structure of ThS_2 at ambient and high-pressure conditions by performing an extensive structure search using first-principles total energy calculations and the particle-swarm optimization (PSO) algorithm¹⁷. Our structure search identifies three viable crystal phases of ThS_2 in $Pnma$, $Fm\bar{3}m$, and $I4/mmm$ symmetry, respectively, and the calculated elastic parameters and phonon dispersions confirm their mechanical and dynamical stability. Further studies of the enthalpy and Helmholtz free energy of these structures reveal a series of pressure-induced structural phase transitions and a temperature-driven phase transition at ambient conditions, which are in good agreement with previously reported experimental observations, and our calculations provide insights into the underlying mechanisms. The calculations also provide key information on the evolution of the structural and electronic properties of these phases. Calculated energetic results show that several structural phases may coexist at high pressures. Electronic band-structure calculations reveal that the highly compressed $Pnma$ phase and the high-pressure $I4/mmm$ phase are both metallic, suggesting an electronic phase transition from the semiconducting state in the low-pressure $Fm\bar{3}m$ and $Pnma$ phases to the metallic state in the high-pressure $Pnma$ and $I4/mmm$ phases. The present results establish key material properties of ThS_2 that are important to both fundamental understanding and practical application of this interesting compound.

The rest of this paper is organized as follows. Section II discusses the details of the computational methods used in the present work. Section III contains the results and discussions of the crystal parameters, equations of state, phonon dispersions, elastic constants and structural and electronic phase transitions induced by pressure or temperature. A summary of our main findings is presented in Section IV.

II. COMPUTATIONAL METHODS

The density-functional-theory (DFT) calculations reported in the present work were carried out using the Vienna *Ab initio* Simulation Package (VASP)^{18,19} with the projector augmented wave scheme (PAW)^{20,21}. The exchange-correlation functional with the generalized gradient approximation (GGA) of Perdew-Burke-Ernzerhof (PBE)²² was used to solve the Kohn-Sham equations with a kinetic energy cutoff of 600 eV. Since none of the localized $5f$ -like bands is occupied in Th, the DFT-GGA level calculations provide adequate description for the structural and vibrational properties of Th and its compounds^{23–26}. We performed global structural optimization for ThS_2 by combining first-principles total energy calculations and the particle-swarm optimization (PSO) algorithm¹⁷ on structural prediction as implemented in the CALYPSO code²⁷, which has been proved to be effective and accurate in predicting the crystal structures of a large variety of materials^{28–35}. The structure

searches were performed using the CALYPSO code with system sizes ranging from 1 to 8 formula units (f.u.) per simulation cell at pressures of 0, 50 and 100 GPa. The structural relaxations were performed allowing the variations of the ionic position, cell volume, and cell shape. The Brillouin-zone (BZ) was sampled with a $12 \times 12 \times 12$ k-point mesh, a $8 \times 12 \times 6$ k-point mesh, and a $12 \times 12 \times 8$ k-point mesh generated via the Monkhorst-Pack scheme³⁶ for the $Fm\bar{3}m$ phase, $Pnma$ phase, and $I4/mmm$ phase, respectively. The geometries were considered to be converged when the forces on each ion became less than 0.001 eV/Å. The convergence threshold was set to be 10^{-7} eV for the total energy calculations in the electronic self-consistent loop. The third-order Birch-Murnaghan equation of state³⁷ was used to fit the calculated results.

We also calculated the phonon dispersion to check for dynamical stability of the crystal structures of various phases of ThS_2 and obtained the corresponding phonon density of states (DOS) that are used as input for calculations of selected thermodynamic functions. These phonon calculations were carried out using a supercell approach³⁸ as implemented in the PHONOPY code³⁹. Supercells of sizes $3 \times 3 \times 3$, $2 \times 3 \times 2$ and $2 \times 2 \times 2$ were created from the optimized crystallographic primitive cell for the $Fm\bar{3}m$ phase, $Pnma$ phase and $I4/mmm$ phase, respectively. The BZ integration was performed with a $2 \times 2 \times 2$ k-point mesh. The symmetry non-equivalent Th and S atoms were displaced from their equilibrium positions by an amplitude of 0.02 Å to construct the system dynamical matrix $D(k)$. The forces induced by small displacements were calculated within VASP.

To study the effect of temperature on the relative stability of the $Fm\bar{3}m$ and $Pnma$ phases of ThS_2 at zero pressure, we have calculated the Helmholtz free energy $F(V, T)$ defined as:

$$F(V, T) = E(V) + F_{vib}(V, T) + F_{el}(V, T), \quad (1)$$

where $E(V)$ is the ground-state total energy, $F_{vib}(V, T)$ is the vibrational energy of the lattice ions and $F_{el}(V, T)$ is the thermal electronic contribution. Since both $Fm\bar{3}m$ and $Pnma$ phases are insulators, the $F_{el}(V, T)$ term makes negligible contributions and can be neglected^{40,41}. The vibrational term $F_{vib}(V, T)$ dominates and is determined by

$$F_{vib}(V, T) = k_B T \int_0^\infty g(\omega) \ln \left[2 \sinh \left(\frac{\hbar \omega}{2 k_B T} \right) \right] d\omega, \quad (2)$$

where $g(\omega)$ is the phonon DOS. This formula strictly requires that all the phonon frequencies ω are positive, and therefore it is not suitable for dynamically unstable phases⁴¹. This condition is satisfied in our calculations since the structural phases of ThS_2 studied in the present work are all dynamically stable in the parameter regions where the thermodynamic properties are examined.

III. RESULTS AND DISCUSSIONS

A. Structure identification and characterization

At ambient conditions, ThS_2 adopts the PbCl_2 -type structure with the space group $Pnma$ ^{13–16} as shown in Fig. 1(b). It is interesting to note that this space group is also adopted by the high-pressure phase of thorium dioxide (ThO_2)^{42–45}. To explore the structural evolution of ThS_2 under pressure, we first pressurize the $Pnma$ phase to investigate the variation of the lattice constants. The calculated lattice constants (a , b and c) as a function of pressure are presented in Fig. 2. The results show that the $Pnma$ phase of ThS_2 is more easily compressible along the a direction than along the b or c directions, indicating that the compression process would be anisotropic. Interestingly, as the pressure reaches around 43 GPa, there is an abrupt decrease in the lattice constant a accompanied by steep increases in the lattice constants b and c . Such a behavior is characteristic of an isostructural phase transition where the space group of a crystalline structure remains unchanged while the lattice constants undergo sudden changes. This phenomenon was also observed in ThO_2 ⁴⁵, UO_2 ⁴⁶ and PuO_2 ^{40,46}. Results in Fig. 2 show that there are two iso-structural phase transitions in the $Pnma$ phase of ThS_2 under compression, one around 43 GPa to a phase termed $Pnma$ -I and the other around 52 GPa to another phase termed $Pnma$ -II.

To explore possible new phases of ThS_2 at high pressures, we have performed an extensive structure search up to 100 GPa using the CALYPSO code. The procedure successfully reproduced the previously known $Pnma$ phase of ThS_2 , and the structure search also identifies two new structures, one in a face-centered-cubic structure with the space group $Fm\bar{3}m$ and the other in a body-centered-tetragonal structure with the space group $I4/mmm$, as illustrated in Fig. 1 (a) and (c), respectively. It is known that the ground-state structure of ThO_2 adopts the $Fm\bar{3}m$ symmetry^{42–45}. We will show below that our energetic calculations also identify the $Fm\bar{3}m$ phase as the ground-state structure for ThS_2 at low temperatures, but the crystal is thermodynamically driven into the $Pnma$ phase around the room temperature, which explains the experimental observation of the $Pnma$ phase of ThS_2 at ambient conditions. The $Fm\bar{3}m$ phase contains four ThS_2 f.u. per unit-cell and each cation in this phase has a coordination number of eight. In the $Fm\bar{3}m$ phase the Th atoms occupy the $4a$ Wyckoff positions (0, 0, 0) and the S atoms occupy the $8c$ Wyckoff positions (0.25, 0.25, 0.25). Meanwhile, the $I4/mmm$ phase of ThS_2 has two f.u. per unit-cell and each cation has a coordination number of ten. In the $I4/mmm$ phase of ThS_2 the Th atoms occupy the $2a$ positions (0, 0, 0) and the S atoms occupy the $4e$ positions (0, 0, 0.344). The calculated lattice constants for these three ThS_2 phases are listed in Table I and compared with available experimental data for the $Pnma$ phase.

TABLE I: Calculated lattice constants of the three ThS_2 phases compared to available experimental data.

	$a_0(\text{\AA})$	$b_0(\text{\AA})$	$c_0(\text{\AA})$	
$Pnma$	7.280	4.300	8.651	Our work
	7.275	4.283	8.617	Exp. ¹⁴
	7.267	4.273	8.615	Exp. ¹⁵
	7.260	4.269	8.600	Exp. ¹⁶
$Fm\bar{3}m$	6.676			Our work
$I4/mmm$	3.751		8.902	Our work

The calculated results are in good agreement with the experimental data^{14–16}.

B. Mechanical and dynamical stability

To determine the mechanical and dynamical stability of the three structural phases of ThS_2 , we have calculated their phonon dispersion curves and elastic constants. The phonon dispersion of a crystal plays a fundamental role in determining the stability of the structure. A dynamical instability of the crystal is associated with soft phonon modes with imaginary frequencies⁴⁷. To check the dynamical stability of the three ThS_2 phases identified by our structure search method, we have calculated their phonon dispersion curves at ambient and high pressures. The results at 0 GPa are shown in Fig. 3, and no imaginary modes were found in the entire Brillouin zone for all three phases of ThS_2 , thus confirming their dynamical stability. Moreover, the calculated phonon dispersions at selected high-pressure points corresponding to the structural phase transitions (see below) shown in Fig. 4 also contain no imaginary modes. These results indicate that the ThS_2 structures are dynamically stable in the entire pressure range studied here, and the absence of any phonon softening at high pressures show that the pressure-induced phase transitions studied below are all driven by the energetics (i.e., the relative enthalpy change) of the system.

The elastic constants measure the response of the crystal structure to external strain, and they also impose constraints on the structural stability. To investigate the mechanical stabilities of the three phases of ThS_2 , we have derived the second-order elastic constants (C_{ij}) from the stress-strain relationship⁴⁸. The calculated results at zero pressure and the selected high-pressure points corresponding to the structural phase transitions are shown in Table II. The mechanical stability of a crystal requires the strain energy to be positive, which implies that the whole set of elastic constants C_{ij} should satisfy the Born-Huang criteria⁴⁹. The $Fm\bar{3}m$ phase is a cubic structure, in which the independent elastic stiffness tensor reduces to three components of C_{11} , C_{44} and C_{12} , and the corresponding mechanical stability criteria are given by⁵⁰ $C_{11} > 0$, $C_{44} > 0$, $C_{11} > |C_{12}|$ and $(C_{11} + 2C_{12}) > 0$. The $Pnma$ phase is an orthorhombic structure, in which the

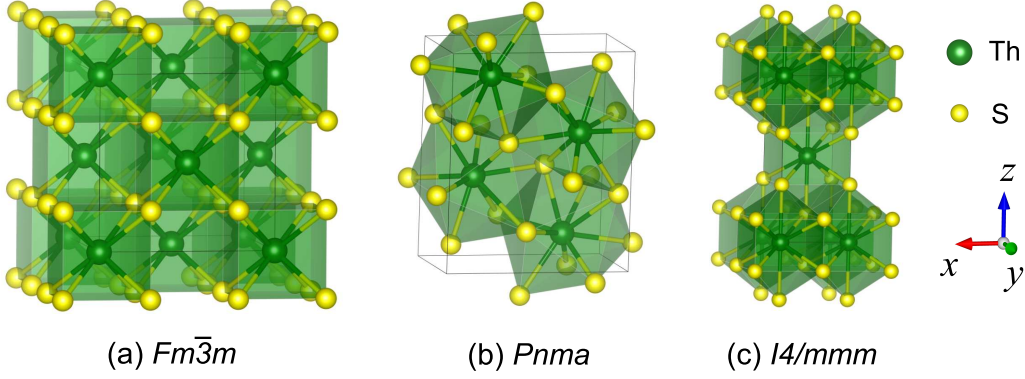


FIG. 1: (Color online) Crystal structures of (a) $Fm\bar{3}m$ phase, (b) $Pnma$ phase and (c) $I4/mmm$ phase of ThS_2 .

TABLE II: Calculated elastic constants C_{ij} (in GPa) for the three ThS_2 phases at zero and the phase transition pressures.

		C_{11}	C_{22}	C_{33}	C_{44}	C_{55}	C_{66}	C_{12}	C_{13}	C_{23}
$Fm\bar{3}m$	0 GPa	169.5			18.3			48.5		
	2.3 GPa	178.2			18.8			54.2		
$Pnma$	0 GPa	148.6	121.1	150.1	46.2	19.3	35.5	64.7	65.7	68.5
	2.3 GPa	156.8	136.0	165.9	51.4	25.6	40.3	73.4	71.3	80.0
	37 GPa	190.7	255.6	288.0	106.3	76.4	77.0	177.6	135.8	156.8
$I4/mmm$	0 GPa	203.0		188.7	81.1		60.0	65.8	54.2	
	37 GPa	306.3		406.8	205.4		129.9	160.6	115.4	

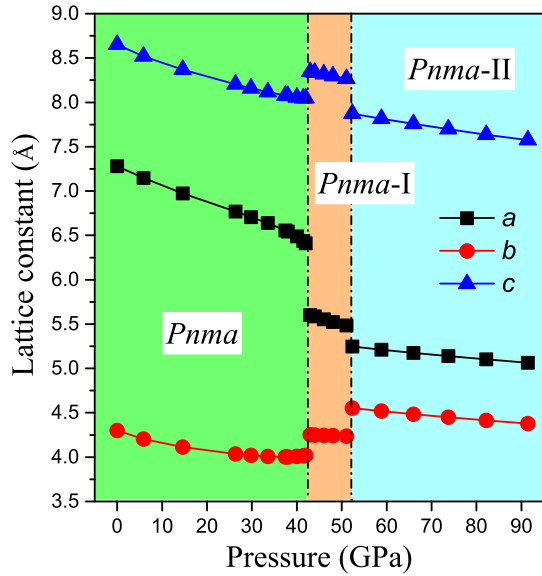


FIG. 2: (Color online) Variation of lattice constants with pressure for the $Pnma$ phase of ThS_2 .

independent elastic stiffness tensor reduces to nine components of C_{11} , C_{22} , C_{33} , C_{44} , C_{55} , C_{66} , C_{12} , C_{13} and C_{23} , and in this case the mechanical stability criteria are given by⁵⁰ $C_{11} > 0$, $C_{22} > 0$, $C_{33} > 0$, $C_{44} > 0$, $C_{55} > 0$,

$C_{66} > 0$, $[C_{11} + C_{22} + C_{33} + 2(C_{12} + C_{13} + C_{23})] > 0$, $(C_{11} + C_{22} - 2C_{12}) > 0$, $(C_{11} + C_{33} - 2C_{13}) > 0$ and $(C_{22} + C_{33} - 2C_{23}) > 0$. The $I4/mmm$ phase is a tetragonal structure, which has six independent elastic constants C_{11} , C_{33} , C_{44} , C_{66} , C_{12} and C_{13} , and the mechanical stability criteria are given by⁵⁰ $C_{11} > 0$, $C_{33} > 0$, $C_{44} > 0$, $C_{66} > 0$, $(C_{11} - C_{12}) > 0$, $(C_{11} + C_{33} - 2C_{13}) > 0$, $[2(C_{11} + C_{12}) + C_{33} + 4C_{13}] > 0$. From the results listed in Table II, the elastic constants C_{ij} for the three ThS_2 phases satisfy their respective mechanical stability criteria at zero and phase transition pressures, thus confirming their mechanical stability. These results further support the conclusion that the phase transitions in ThS_2 are driven by the energetics of the system. It is noted that there is a crossover between the C_{11} and C_{22} in Table II. This is due to the anisotropy effect of the $Pnma$ phase under pressure, i.e., it is easier to compress the structure along the y and z direction than along the x direction.

C. Equation of state and structural phase transitions

We have calculated the energy versus volume relations for the three phases of ThS_2 , and the obtained results fitted by the third-order Birch-Murnaghan equation are shown in Fig. 5. The calculations reveal that the $Fm\bar{3}m$ phase is energetically the most favorable among the three phases, and an inspection of the common tangent of these

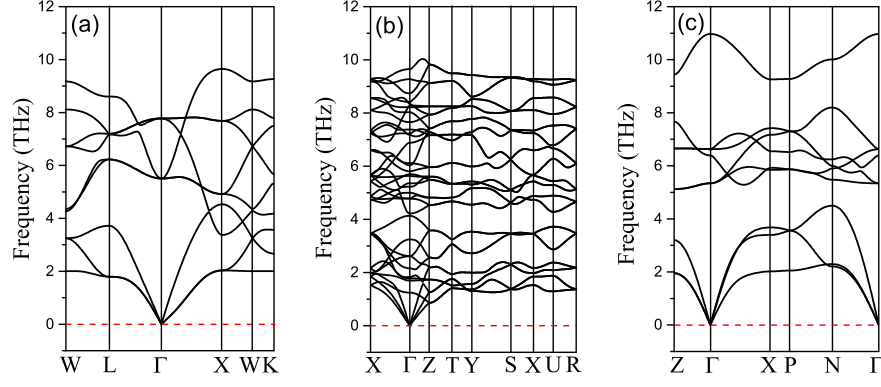


FIG. 3: (Color online) Phonon dispersion curves for (a) $Fm\bar{3}m$, (b) $Pnma$ and (c) $I4/mmm$ phase of ThS_2 .

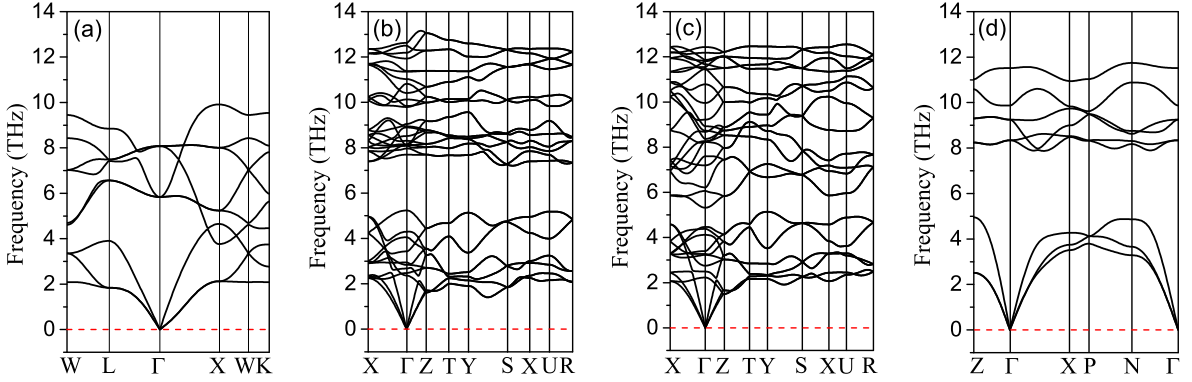


FIG. 4: (Color online) Phonon dispersion curves for (a) $Fm\bar{3}m$ - ThS_2 at 2.3 GPa, (b) $Pnma$ - ThS_2 at 37 GPa, (c) $Pnma$ -I- ThS_2 at 43 GPa and (d) $I4/mmm$ - ThS_2 at 37 GPa.

energy versus volume curves suggests a pressure-induced structural phase transition from the $Fm\bar{3}m$ phase to the $Pnma$ phase at a relatively low pressure, followed by a phase transition from the $Pnma$ phase to the $I4/mmm$ phase at a higher pressure. This is indeed confirmed by the calculated enthalpy versus pressure results shown in the inset of Fig. 5, which predict a transition from the $Fm\bar{3}m$ phase to the $Pnma$ phase at 2.3 GPa and a subsequent transition from the $Pnma$ phase to the $I4/mmm$ phase at 37 GPa. We also performed calculations to construct the volume-pressure relation for the three phases of ThS_2 , and the obtained results are shown in Fig. 6. It is seen that the structural transitions between the various ThS_2 phases are accompanied by significant volume collapses. We have extracted the bulk modulus for the ThS_2 phases by fitting the calculated results to the third-order Birch-Murnaghan equation of state, and the obtained results are 89 GPa, 86 GPa, and 107 GPa for the $Fm\bar{3}m$, $Pnma$, and $I4/mmm$ phases of ThS_2 , respectively. We also determined the bulk modulus of these phases from the calculated elastic constants, and the obtained results are practically identical to those from fitting the equation

of state.

We now connect our calculated results to the reported experimental observations. We first examine the structural stability of ThS_2 . According to the calculated total-energy results shown in Fig. 5, the $Fm\bar{3}m$ phase is energetically the most stable among the three phases of ThS_2 . Experimentally, however, only the $Pnma$ phase was observed^{13–16} at ambient conditions. To elucidate the underlying mechanism, we have calculated the Helmholtz free energy $F(V, T)$ of the $Fm\bar{3}m$ and the $Pnma$ phase over the relevant temperature range. The obtained results shown in Fig. 7 indicate that the $Fm\bar{3}m$ phase is the ground-state structure below 280 K, but above this transition temperature the $Pnma$ phase becomes thermodynamically more stable. Our calculations therefore reveal a temperature-driven structural phase transition in ThS_2 , explaining the experimental observation of the $Pnma$ phase at the ambient temperature; the predicted stability of the $Fm\bar{3}m$ phase as the ground-state phase at temperatures below 280 K expands the structural phase diagram of ThS_2 , and this prediction calls for further experimental verification and exploration.

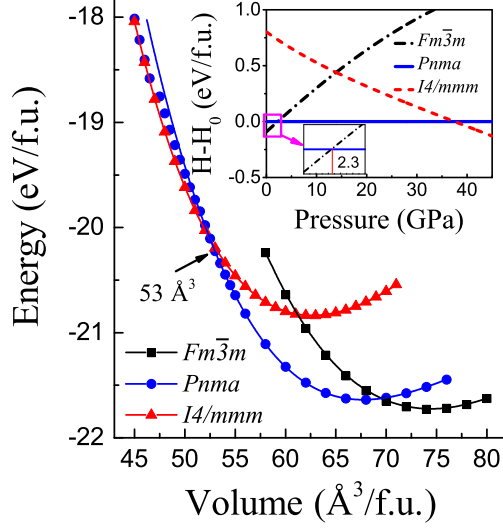


FIG. 5: (Color online) Total energy versus volume results for the $Fm\bar{3}m$ phase, $Pnma$ phase and $I4/mmm$ phase of ThS_2 . The symbols represent our calculated data points and the solid lines are the fitting curves of the third-order Birch-Murnaghan equation. The inset shows the enthalpy versus pressure curves with the enthalpy of the $Pnma$ phase set to zero as the reference. It is noted that the E-V equation of state and the enthalpy of $Pnma$ phase are derived from the E-V data of the $Pnma$ phase ($53 \sim 76 \text{ \AA}^3$), without using any points of the $Pnma$ -I and $Pnma$ -II phases.

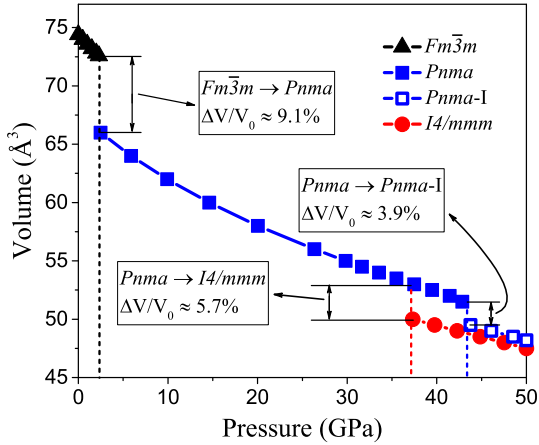


FIG. 6: (Color online) The calculated volume versus pressure relation for the three phases of ThS_2 . The relative volume change at each pressure where a volume collapse occurs is measured against the initial volume V_0 right before each volume drop.

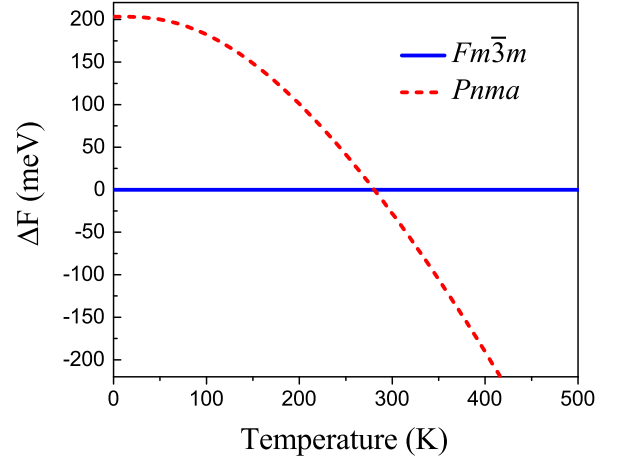


FIG. 7: (Color online) Temperature dependence of the Helmholtz free energy of the $Pnma$ phase of ThS_2 measured relative to that of the $Fm\bar{3}m$ phase.

It has been reported¹⁶ that ThS_2 undergoes a pressure-induced, sluggish structural phase transition around 40 GPa, but the details about the nature of the phase transition and the characterization of the high-pressure phase need further examination and clarification. Our calculated enthalpy versus pressure results shown in the inset of Fig. 5 indicate a transition from the $Pnma$ phase to the $I4/mmm$ phase at 37 GPa, which is close to the experimentally reported transition pressure of about 40 GPa. Furthermore, during this phase transition, the volume of the $Pnma$ phase is compressed to $53 \text{ \AA}^3/\text{f.u.}$, and in a large range of volume under further compression, the total energy of the $Pnma$ phase remains very close to that of the $I4/mmm$ phase as seen in Fig. 5. Eventually, the E-V curve of the $Pnma$ phase nearly coincides with that of the $I4/mmm$ phase after the kink at around 47 \AA^3 . This kink corresponds to the iso-structural phase transition from the $Pnma$ -I to the $Pnma$ -II phase (see Fig. 5 and Fig. 2). This close energetic relation suggests that these two phases may coexist during the compression process, thus making the phase transition sluggish as observed in the experiment. It is interesting to note (see Fig. 2) that the $Pnma$ phase undergoes a transformation to an isostructural $Pnma$ -I phase at about 43 GPa. It is therefore expected that there might be multiple phases coexisting around 40 GPa where several structural and electronic (see below) phase transitions occur. The simultaneous presence of the highly compressed $Pnma$ and $I4/mmm$ phases together with the transformed (or partially transformed) $Pnma$ -I phase could complicate the determination of the structural details near the phase transition pressure, and the theoretical results obtained here may offer a useful guidance to sort out the structural details.

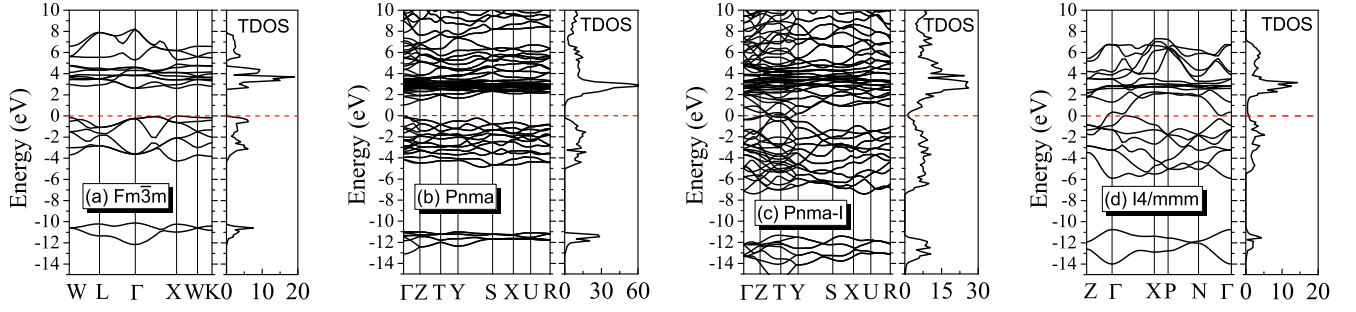


FIG. 8: (Color online) Electronic band structures and total density of states (TDOS) for (a) $Fm\bar{3}m$ phase, (b) $Pnma$ phase, (c) $Pnma$ -I phase (44 GPa) and (d) $I4/mmm$ phase of ThS_2 .

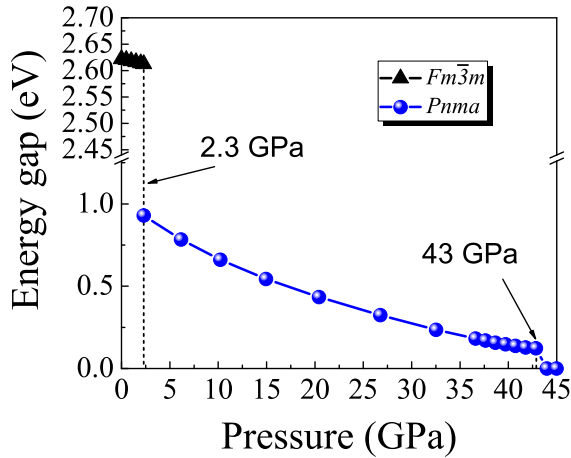


FIG. 9: (Color online) The electronic bandgap versus pressure for the $Fm\bar{3}m$ and $Pnma$ phases of ThS_2 .

D. Pressure-induced semiconductor-metal transitions

The electronic properties of ThS_2 are also expected to be sensitive to the applied pressure. We have calculated the electronic band structures of the three phases of ThS_2 studied here and investigated the evolution of the electronic bandgap with increasing pressure. We first determined the band structures at zero pressure. The results in Fig. 8 show that the $Fm\bar{3}m$ phase is a semiconductor with an indirect band gap of 2.622 eV, and the top of the valence band and the bottom of the conduction band are located at the X point and the Γ point, respectively. Meanwhile, the $Pnma$ phase is also a semiconductor but with a direct band gap of 1.037 eV, and both the top of the valence band and the bottom of the conduction band are located at the Γ point. On the other hand, the $I4/mmm$ phase is in a metallic state. It is noted that our calculated bandgap values for the $Fm\bar{3}m$ and $Pnma$ phase may have been underestimated by the use of the PBE/GGA exchange-correlation functional and, there-

fore, the actual bandgaps for these phase are likely to be larger than those reported here. However, the metallic nature of the $I4/mmm$ phase is unlikely to be affected since the steep band crossing near the Fermi energy, which is mainly contributed by the S- p electrons, is not sensitive to the choice of the potential used, and calculations using more accurate hybrid functionals are not known to open a bandgap in systems with such steep band crossings at the Fermi level. We have performed further systematic band-structure calculations and determined the bandgap variation with increasing pressure. The obtained bandgap values for the $Fm\bar{3}m$ and $Pnma$ phases of ThS_2 as a function of pressure are presented in Fig. 9. The results show that the bandgap of the $Fm\bar{3}m$ phase decreases slightly with increasing pressure. Then at the transition from the $Fm\bar{3}m$ to the $Pnma$ phase, which should be observable at low temperatures (below 280 K), there is a significant drop in the bandgap from about 2.6 eV to about 0.9 eV. At further increased pressure, the bandgap of the $Pnma$ phase decreases gradually until 43 GPa where the bandgap collapses when the system transitions from the semiconducting $Pnma$ phase to the metallic $Pnma$ -I phase (its electronic band structure is shown in Fig. 8(c)). It is noted, however, that this semiconductor-metal transition accompanying the isostructural phase transition in the $Pnma$ symmetry may be preceded by another semiconductor-metal transition at 37 GPa following the structural transition from the $Pnma$ phase to the $I4/mmm$ phase, since the latter phase remains metallic in the entire pressure range studied here.

IV. SUMMARY

In this work we have conducted a systematic study of ThS_2 using a host of current computational techniques to examine the structural, electronic, lattice dynamics, and thermodynamic properties that are important to the fundamental understanding and practical applications. Our structure search has successfully identified the experimentally observed $Pnma$ phase of ThS_2 and pre-

dicted two new structures, the $Fm\bar{3}m$ phase that exist as the ground-state structure at low-pressure and low-temperature conditions and the $I4/mmm$ phase that becomes energetically favorable at high pressures. Based on the calculated results of the Helmholtz free energy for the ThS_2 phases, we find a temperature-driven phase transition at 280 K from the $Fm\bar{3}m$ phase to the $Pnma$ phase, which explains the experimental observation of the $Pnma$ phase at the ambient conditions. Our enthalpy calculations predict a structural phase transition from the $Pnma$ phase to the $I4/mmm$ phase at 37 GPa, which is in good agreement with the experimental observation of a phase transition around 40 GPa, and the obtained results also provide a full characterization of the nature and details about the pressure-induced structural phase transition of ThS_2 . In particular, the close energetics of several structural phases, including the original $Pnma$ phase, one of its isostructural variations, and the $I4/mmm$ phase, around the phase transition pressure suggest their possible coexistence, which provides an explanation for the experimentally observed sluggishness of the transition and the difficulty in identifying the structural details from the previously collected experimental data alone. The calculated results presented in this work may help further resolve the pressure-induced structural evolution and phase transitions of ThS_2 . Moreover, our electronic band structure calculations reveal a series of pressure-induced electronic phase transitions from the semiconducting state in the low-pressure $Fm\bar{3}m$ and $Pnma$ phases to the metallic state in the high-pressure $Pnma$ and $I4/mmm$ phases.

The results reported here provide a comprehensive description of a variety of physical properties of ThS_2 over a wide range of pressure and temperature conditions and set key benchmarks for the characterization and further assessment of this compound. These results explain existing experimental observations and offer insights for understanding the mechanisms underlying the variations of the structural and electronic properties of ThS_2 . Such insights are crucial to evaluating the behavior and determining the role of ThS_2 in various applications, including the thorium fuel reprocessing cycle. The theoretical predictions about the new structural phases and the electronic phase transitions in the pressure-temperature phase space of ThS_2 call for further experimental verification and exploration.

Acknowledgments

This work is partially supported by the National Natural Science Foundation of China (Grant Nos. 91326105, 11574333, and U1532124), and the Strategic Priority Research Program of the Chinese Academy of Sciences (Grant No. XDA02040100). C.F.C. was supported in part by the DOE under Cooperative Agreement No. DE-NA0001982. The TMSR supercomputer center, the Supercomputing Center, CAS, and the Shanghai Supercomputing Center are acknowledged for allocation of computing time.

-
- * Electronic address: xzke@phy.ecnu.edu.cn
 † Electronic address: huaiping@sinap.ac.cn
 ‡ Electronic address: chen@physics.unlv.edu
- ¹ S. F. Ashley, G. T. Parks, W. J. Nuttall, C. Boxall and R. W. Grimes, *Nature* **429**, 31-33, (2012).
 - ² See <http://www.world-nuclear.org/info/Nuclear-Fuel-Cycle/Uranium-Resources/Supply-of-Uranium/> (2015).
 - ³ A. Gale, C. A. Dalton, C. H. Langmuir, Y. Su, and J.-G. Schilling, *Geochem. Geophys. Geosyst.* **14**, 489 (2013).
 - ⁴ M. B. Andersen, T. Elliott, H. Freymuth, K. W. W. Sims, Y. Niu, and K. A. Kelley, *Nature* **517**, 356 (2015).
 - ⁵ P. Bagla, *Science* **350**, 726 (2015).
 - ⁶ R. W. Grimes and W. J. Nuttall, *Science* **329**, 799 (2010).
 - ⁷ S. Hirai, K. Shimakage, Y. Saitou, T. Nishimura, Y. Uemura, M. Mitomo and L. Brewer, *J. Am. Ceram. Soc.* **81**, 145 (1998).
 - ⁸ M. Ohta, H. Yuan, S. Hirai, Y. Uemura and K. Shimakage, *J. Alloy. Comp.* **374**, 112 (2004).
 - ⁹ N. Sato, G. Shinohara, A. Kirishima and O. Tochiyama, *J. Alloy. Comp.* **451**, 669 (2008).
 - ¹⁰ N. Sato and A. Kirishima, *Energy Procedia* **7**, 444 (2011).
 - ¹¹ N. Sato and A. Kirishima, *J. Nucl. Mater.* **414**, 324 (2011).
 - ¹² M. Ohta, S. Satoh, T. Kuzuya, S. Hirai, M. Kunii and A. Yamamoto, *Acta Mater.* **60**, 7232 (2012).
 - ¹³ E. D. Eastman, L. Brewer, L. A. Bromley, P. W. Gilles, and N. L. Lofgren, *J. Am. Chem. Soc.* **72**, 4019 (1950).
 - ¹⁴ J. Graham and F. McTaggart, *Aust. J. Chem.* **13**, 67 (1960).
 - ¹⁵ G. Amoretti, G. Calestani, and D. C. Giori, *Z. Naturforsch. A* **39**, 778 (1984).
 - ¹⁶ L. Gerward, J. Staun Olsen, U. Benedict, H. C. Abraham, and F. Hulliger, *High Press. Res.* **13**, 327 (1995).
 - ¹⁷ Y. Wang, J. Lv, L. Zhu, and Y. Ma, *Phys. Rev. B* **82**, 094116 (2010).
 - ¹⁸ G. Kresse and J. Furthmüller, *Phys. Rev. B* **54**, 11169 (1996).
 - ¹⁹ G. Kresse and J. Furthmüller, *Comput. Mater. Sci.* **6**, 15 (1996).
 - ²⁰ P. E. Blöchl, *Phys. Rev. B* **50**, 17953 (1994).
 - ²¹ G. Kresse and D. Joubert, *Phys. Rev. B* **59**, 1758 (1999).
 - ²² J. P. Perdew, K. Burke, and M. Ernzerhof, *Phys. Rev. Lett.* **77**, 3865 (1996).
 - ²³ L. A. Koscielski, E. Ringe, R. P. Van Duyne, D. E. Ellis, and J. A. Ibers, *Inorg. chem.* **51**, 8112 (2012).
 - ²⁴ I. R. Shein, K. I. Shein, and A. L. Ivanovskii, *J. Nucl. Mater.* **353**, 19 (2006).
 - ²⁵ D. Pérez Daroca, S. Jaroszewicz, A. M. Llois, and H. O. Mosca, *J. Nucl. Mater.* **437**, 135 (2013).
 - ²⁶ Y.-L. Guo, W.-J. Qiu, X.-Z. Ke, P. Huai, C. Cheng, H. Han, C.-L. Ren, and Z.-Y. Zhu, *Phys. Lett. A* **379**, 1607 (2015).
 - ²⁷ Y. Wang, J. Lv, L. Zhu, and Y. Ma, *Comput. Phys. Com-*

- mun. **183**, 2063 (2012).
- ²⁸ J. Lv, Y. Wang, L. Zhu, and Y. Ma, Phys. Rev. Lett. **106**, 015503 (2011).
 - ²⁹ L. Zhu, H. Wang, Y. Wang, J. Lv, Y. Ma, Q. Cui, Y. Ma, and G. Zou, Phys. Rev. Lett. **106**, 145501 (2011).
 - ³⁰ H. Liu and Y. Ma, Phys. Rev. Lett. **110**, 025903 (2013).
 - ³¹ D. Zhou, Q. Li, Y. Ma, Q. Cui, and C. F. Chen, J. Phys. Chem. C **117**, 5352 (2013).
 - ³² Q. Li, D. Zhou, W. Zheng, Y. Ma, and C. F. Chen, Phys. Rev. Lett. **110**, 136403 (2013).
 - ³³ M. Zhang, H. Liu, Q. Li, B. Gao, Y. Wang, H. Li, C. F. Chen, and Y. Ma, Phys. Rev. Lett. **114**, 015502 (2015).
 - ³⁴ Q. Li, D. Zhou, W. Zheng, Y. Ma, and C. F. Chen, Phys. Rev. Lett. **115**, 185502 (2015).
 - ³⁵ L. Bai, Q. Li, S. A. Corr, M. Pravica, C. F. Chen, Y. Zhao, S. V. Sinogeikin, Y. Meng, C. Park, and G. Shen, Phys. Rev. B **92**, 134106 (2015).
 - ³⁶ H. J. Monkhorst and J. D. Pack, Phys. Rev. B **13**, 5188 (1976).
 - ³⁷ F. Birch, J. Geophys. Res. **91**, 4949 (1986).
 - ³⁸ K. Parlinski, Z. Q. Li, and Y. Kawazoe, Phys. Rev. Lett. **78**, 4063 (1997).
 - ³⁹ A. Togo, F. Oba, and I. Tanaka, Phys. Rev. B **78**, 134106 (2008).
 - ⁴⁰ P. Zhang, B.-T. Wang, and X.-G. Zhao, Phys. Rev. B **82**, 144110 (2010).
 - ⁴¹ B.-T. Wang, P. Zhang, R. Lizárraga, I. Di Marco, and O. Eriksson, Phys. Rev. B **88**, 104107 (2013).
 - ⁴² J.-P. Dancausse, E. Gering, S. Heathman, and U. Benedict, High Press. Res. **2**, 381 (1990).
 - ⁴³ M. Idiri, T. Le Bihan, S. Heathman, and J. Rebizant, Phys. Rev. B **70**, 014113 (2004).
 - ⁴⁴ B.-T. Wang, H. Shi, W.-D. Li, and P. Zhang, J. Nucl. Mater. **399**, 181 (2010).
 - ⁴⁵ H. X. Song, L. Liu, H. Y. Geng, and Q. Wu, Phys. Rev. B **87**, 184103 (2013).
 - ⁴⁶ H. X. Song, H. Y. Geng, and Q. Wu, Phys. Rev. B **85**, 064110 (2012).
 - ⁴⁷ W. Cochran, Phys. Rev. Lett. **3**, 412 (1959).
 - ⁴⁸ Y. Le Page and P. Saxe, Phys. Rev. B **65**, 104104 (2002).
 - ⁴⁹ M. Born and K. Huang, Dynamical Theory of Crystal Lattices Oxford Classic Texts in the Physical Sciences (Clarendon Press, Oxford, 1988).
 - ⁵⁰ Z.-J. Wu, E.-J. Zhao, H.-P. Xiang, X.-F. Hao, X.-J. Liu, and J. Meng, Phys. Rev. B **76**, 054115 (2007).